Title: Spatially Resolved Raman Spectroscopy of Thin Carbon Interphase in SiC Ceramic Matrix Composites*

Authors: Yuki Jimba (jimbay@ornl.gov), Benjamin Lamm (lammbw@ornl.gov), Takaaki Koyanagi (koyanagit@ornl.gov)

Affiliation: Materials Science and Technology Division, Oak Ridge National Laboratory, Oak Ridge, Tennessee, USA

Abstract:

A dedicated analysis method is presented to extract the Raman spectrum of an interphase layer thinner than the laser spot size. We focused on spatial correlations between the contrast of optical micrographs and Raman hyperspectral data to predict the constituents of the mixed spectra measured near the interphase. By employing a mapping step size of 0.1 μm, the Raman spectrum of approximately 0.3 μm thick carbon interphase in a SiC fiber reinforced SiC matrix composite was extracted from data acquired with a theoretical spot size of about 0.7 μm. Notably, conventional chemometrics procedures were unable to isolate the interphase signal, instead producing a spectrum representing a mixture of interphase and matrix. This study used another composite with approximately 0.9 μm thick interphase to validate the analysis method, enabling direct measurement of the interphase spectrum. The proposed Raman analysis method has advantages in specimen volume and turnaround time compared to traditional characterization methods, such as transmission electron

microscopy. This study also evaluates applicability of the analysis method to different composite materials and identifies key requirements of the measurements, including the ratio of interphase thickness to spot size and the homogeneity of the surrounding matrix.

Keywords: silicon carbide, ceramic matrix composite, interphase, pyrolytic carbon

Correspondence:

Yuki Jimba, Materials Science and Technology Division, Oak Ridge National Laboratory, 1 Bethel Valley Road, B-155 Building 4500S, Oak Ridge, TN 37831 USA.

Email: jimbay@ornl.gov

Funding information:

US Department of Energy, Office of Fusion Energy Sciences, Fusion Materials Program, and Early Career Research Program under contact DE-AC05-00OR22725 with UT-Battelle LLC.

US Department of Energy Office of Nuclear Energy, Advanced Fuels Campaign under Contract No. DEAC05-00OR22725 with UT-Battelle, LLC.

Conflict of interest:

The authors declare no conflicts of interest.

1. Introduction

Continuous ceramic fiber-reinforced ceramic matrix composites exhibit relatively high fracture toughness due to pseudo-ductile fracture behavior, in contrast to the catastrophic failure typically seen in monolithic ceramics. The fiber-matrix interface plays a critical role in the toughening mechanisms: interfacial bonding must be strong enough to transfer loads between the fiber and the matrix yet weak enough to allow microcracks in the matrix to deflect at the interface [1]. Refractory SiC fiber-reinforced SiC composites (SiC/SiC composites) [2] are used in turbine blades for aircraft engines and are also widely considered for structural materials in nuclear systems and fusion reactors [3-7]. Figure. 1 shows typical cross-sectional microstructures of SiC/SiC composites with a thin layer of pyrolytic carbon (PyC) interphase between the SiC fibers and the SiC matrix [8]. The mechanical and thermal properties of this PyC layer play critical roles in determining the performance of SiC/SiC composites [9-11]. Analysis of the PyC microstructure would help predict its physical and mechanical properties [12].

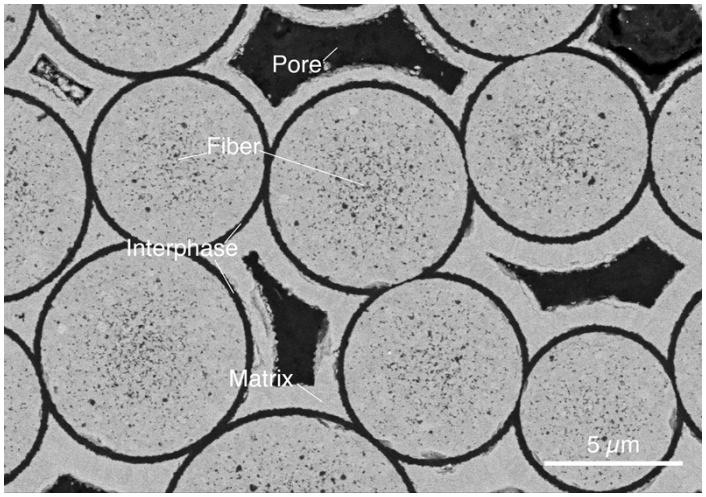

Fig. 1. Backscattered electron micrograph of a cross section of SiC/SiC composite: Tyranno SA3 SiC fiber coated with carbon interphase [8].

Observations of the microstructure of the PyC interphase in SiC/SiC composites are often conducted using transmission electron microscopy (TEM) to characterize approximately 100 nm thick lamellae fabricated by focused ion beam [13-18]. Due to the small specimen volume required for TEM, several TEM specimens would be needed to capture intrinsic heterogeneous microstructure of the SiC/SiC composite interface. Although TEM enables direct observation and measurement of the atomic arrangement [13-15] and electric states [16-18] of the PyC layer, TEM has limitations in turnaround time and cost from the perspective of obtaining information thoroughly from a large volume. Scanning electron microscopy (SEM) combined with energy-dispersive X-ray spectroscopy and wavelength-dispersive X-ray spectroscopy can probe millimeter-scale surfaces but struggles to provide detailed crystallographic information and bond conditions, except when using specialized equipment such as soft X-ray emission spectrometers [19,20].

Raman spectroscopy has been widely employed to assess the microstructure and properties—including crystalline phases [21,22], crystallite size [23,24], elastic strain [25-27], residual stress of fiber-reinforced composites[28], mechanical properties [29], and amorphous-like nanostructure [30-33] – of carbonaceous compounds and SiC in various forms. Hence, Raman spectroscopy offers potential for revealing the structure of PyC. One of the current challenges is to measure the spectrum of the PyC interphase with a thickness of at most 0.5 μm without the PyC spectra being affected by the surrounding materials. A spot diameter of incident light in conventional Raman spectrometers is approximately 1 μm with a high-magnification objective. This is close

to the diffraction limit of light [34,35], and achieving nanoscale spatial resolution with a conventional optical system is challenging. When centered on a 0.5 μm thick PyC interphase layer, a Raman laser spot size of 1 μm yields a mixed spectrum combining the PyC layer, the matrix material, and the fiber material, ultimately requiring deconvolution processes to isolate the PyC layer. One method for measuring Raman spectra in nanoscale regions is the tip-enhanced Raman scattering (TERS) technique, which uses an atomic force microscopy (AFM) probe [36,37]. In TERS, incident light is directed onto the tip of the AFM probe through the objective lens, enabling Raman spectroscopy with high spatial resolution up to tens of nanometers, surpassing the diffraction limit of light. Despite this advantage, TERS is constrained by lengthy acquisition times, making it unsuitable for characterizing larger regions on the millimeter scale. This study explores improvements to data analysis by using a conventional Raman spectroscopy system to extract information about the PyC interphase microstructure from mixed Raman spectra.

Chemometric techniques such as principal component analysis (PCA) and multivariate analysis techniques are widely used in Raman spectroscopy, particularly in the fields of biology, agronomy, and cultural heritage, where they are applied to handle complex spectral overlap from highly variable compounds and to extract meaningful signals from low-quality data acquired with portable instruments[38-42]. In contrast, the application of chemometric methods in materials science has been more limited, with notable exceptions such as their use in the analysis of graphene[43]. However, the increasing structural complexity of modern functional and structural materials – including particle-

or fiber-reinforced ceramic composites – has heightened the importance of accurate interfacial characterization. In this context, applying chemometric approaches to spatially mixed Raman data from micro-scale regions offers a promising strategy for extracting information.

PCA is commonly employed as a data processing technique in conventional Raman spectroscopy for analyzing materials with multiple phases [44,45]. PCA is a statistical method designed to reduce data dimensionality while preserving as much of the original information as possible [46]. Shinzawa et al. have provided a comprehensive overview of the application of PCA in Raman spectroscopy, highlighting its use in chemometric analysis of multiphase samples [47]. The core assumption of PCA is that variations within the dataset contain valuable information, and some variables may be redundant or unnecessary for explaining this information. Principal components (PCs) are calculated as linear combinations of the original variables – in this case, the measured wavenumbers – and are ranked based on the variance they account for in the data, with the first PC (PC1) explaining the largest portion of variance. PC2 is then defined to explain the maximum remaining variance and is orthogonal to PC1. Typically, only a few PCs are needed to capture most of the information within a dataset. Although the PCs do not have direct physical significance, PCA has been widely used since the early 20th century because it can provide objective analysis results in a short period of time without requiring complex parameter settings [47-49]. The conventional PCA approach may not result in reasonable spectral separation when the single-phase signals cannot be detected. In materials that contain thin layers or fine particles of sizes on the order of

hundreds of nanometers, only mixed signals from the matrix and the layer or dispersed particles are measured. PCA often captures these mixed signals as features and outputs them as PCs [50,51]. Because PCA does not have any prior information about the material itself, it may interpret this mixed information incorrectly and lacks the means to correct it. Other unsupervised chemometric methods, including self-modeling curve resolution [47], nonnegative matrix factorization [52], and multivariate curve resolution [53], have also been applied to similar problems. Like PCA, these methods face challenges when the spectral features (e.g., peak positions) of the constituent phases are closely overlapping. As a result, extracting a single-phase spectrum is nontrivial when pure-phase signals are not directly observed.

To overcome the challenges in PCA, a spectrum-extraction method was developed to separate spatially resolved Raman spectra of PyC interphases that are thinner than the laser spot size from mixed spectra. Raman spectral mapping was conducted using a theoretical spot diameter of about 0.7 μm on two types of SiC/SiC composites with different types of fibers, and spectra were analyzed to extract the spectra of 0.3–0.7 μm thick PyC interphases by taking advantage of a small measurement step size of 0.1 μm.

2. Methods

2.1 Experimental Methods

Two types of SiC/SiC composites were used for the Raman spectroscopy: (1) SiC/SiC grown by chemical vapor infiltration (CVI) with 2D satin-weave Tyranno SA3 SiC fiber

reinforcement in a 0°/90° stacking configuration (SA3/SiC), and (2) a 0°/90° cross-ply laminated CVI SiC/SiC composite with SCS-Ultra SiC fiber (SCS/SiC). Figure 2 shows a typical cross-sectional micrograph of SA3/SiC composite. The fiber/matrix interphase was PyC for all composites. The CVI process was conducted by Rolls-Royce High Temperature Composites Inc. (lot number:13C-529). The estimated fiber volume fraction was about 40%, and porosity was 8–16%. The SiC/SiC composite plates were machined with a low-speed diamond saw. Then, the cross sections were mechanically polished using diamond suspensions for the initial stages and colloidal silica suspensions for the final polishing.

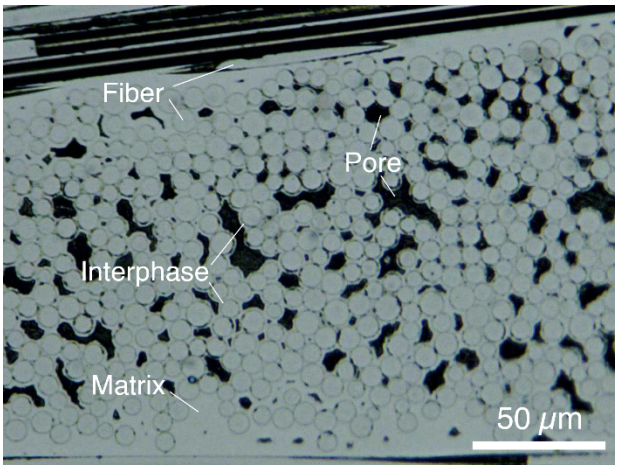

Fig. 2. Cross-sectional optical micrograph of SA3/SiC composites.

The SA3 fiber is a near-stoichiometric SiC fiber consisting of crystalline β-SiC (also known as 3C-SiC) and a free carbon phase [54]. The nominal fiber diameter is 7.5 μm, and the SiC grain size is about 200 nm [55]. SCS was formed by growing SiC by chemical vapor deposition (CVD) onto a carbon core with a diameter of about 35 μm. The nominal SCS fiber diameter was 140 μm. The CVD SiC phase near both the carbon

core and outer surface was reported to be carbon-rich SiC [56,57]. The PyC interphases for both fibers were prepared by Rolls-Royce High Temperature Composites Inc. with thicknesses of 200–350 nm for the SA3/SiC composite and 500–700 nm for the SCS/SiC composite. Further material properties were investigated and are reported elsewhere [8].

Raman spectral mapping was conducted on the polished cross sections of the composites using a Horiba Scientific LabRAM HR Evolution Confocal Raman Microscope equipped with a 532 nm argon ion laser, which was operated at a power of 15 mW at the specimen surface. Spectra were acquired in the range of 385–2037 cm^{-1}. For the Raman mapping experiments, a step size of 0.1 μm was maintained in both the *x* and *y* directions. A 100× objective lens with a nominal numerical aperture of 0.90 was employed. The laser was focused to a theoretical spot diameter of 721 nm on the specimens, as calculated by the Rayleigh criterion [58] based on the wavelength and the nominal numerical aperture. The polished cross sections of the composites were observed using a TESCAN MIRA scanning electron microscope.

2.2. Data processing

The analysis of the fine Raman map data identified data points for a scenario illustrated in Fig. 3(a), where the incident laser interacts only with the matrix and the PyC, named on-edge. In this scenario, the PyC signal is isolated by subtracting the reference spectrum of the matrix from the mixed spectrum. Depending on the type of fiber, carbon

may also be present within the fibers [27,59], complicating the separation of signal of carbon of the fiber from that of the PyC. The CVI SiC matrix is relatively pure SiC, and signals from free carbon are typically minimal in regions adjacent to the PyC. Thus, PyC spectrum extraction is expected to be more straightforward on the matrix + PyC side than on the fiber + PyC side.

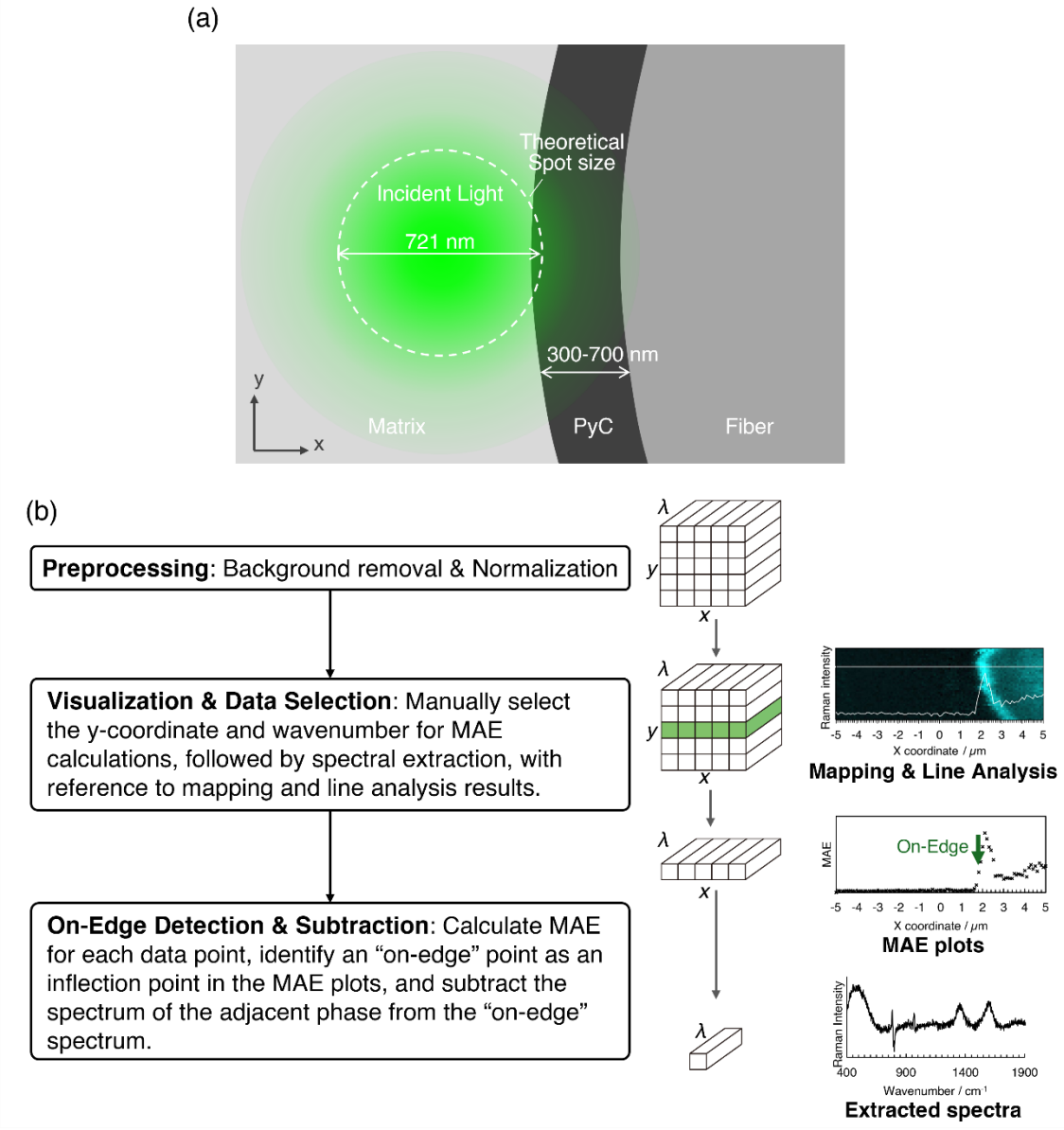

Fig. 3. (a) Illustration of the on-edge scenario and (b) flow chart depicting the data processing, including schematics for spectral extraction from hyperspectral image data set.

A flow chart for this data processing method is shown in Fig. 3(b). This method extracts the spectrum of PyC by sequentially performing preprocessing, visualization and data selection, calculation of the mean absolute error (MAE) of spectra to the reference spectrum of matrix, and subtraction. The initial preprocessing steps involve cosmic ray removal, background subtraction, normalization of the raw spectra based on maximum intensity between 960 and 980 cm^{-1} corresponding to the SiC longitudinal optical (LO) band. MAE is calculated using Eq. (1) [60]:

$$MAE = \frac{1}{n}\sum_{i=1}^{n} |I_i(x) - I_i(reference)| \quad \#(1)$$

where *i* corresponds to the number associated with the wavenumber, and $I_i(x)$ is the Raman intensity at the wavenumber corresponding to *i* at coordinate *x*. The integer *i* ranges from 1 to 1024, corresponding to wavenumbers between 386.183 and 2037.66 cm^{-1}, divided into 1024 steps. A univariate spline was fitted to the MAE values as a function of *x*-coordinate ($R^2 > 0.99$) to identify the inflection points in the resulting trend. In the visualization and data selection steps, a mapping image of the preprocessed data at an arbitrary wavenumber and a line analysis result at the wavenumber at an arbitrary *y*-coordinate is visualized. The data corresponding to the selected *y*-coordinate is used in the subsequent steps. First, in the on-edge detection and subtraction steps, MAE is calculated for each data point, with coordinate *x* using the spectrum of the matrix that is farthest from the PyC as the reference spectrum. To

detect the presence of the PyC signal, the MAE calculation is specifically performed over the range of ±10 cm^{-1} of the wavenumbers selected in the previous step and is plotted against the *x*-coordinates. As the *x*-coordinate progresses from left to right, MAE increases, indicating a change in the Raman intensity at the selected wavenumber. By detecting the point at which the MAE begins to increase, a location is identified where the incident laser interacts with both the matrix and the PyC, referred to as on-edge, as shown in Figs. 3(a) and (b). Finally, the PyC spectrum can be isolated by subtracting the reference spectrum measured at the adjacent matrix from the spectrum obtained at the on-edge coordinate. This process was implemented using a Python script executed in Anaconda Python 3. The code is available on a GitHub repository [61].

Routine data processing, including cosmic ray and background removal, was performed using the Horiba Scientific LabSpec 6 Spectroscopy Suite Software. For the background removal, a 7th-degree polynomial baseline was fitted and subtracted from each spectrum. Conventional chemometrics procedures were also conducted on the processed data for comparison purposes using the Horiba Scientific χSTaiN Instant Raman Analysis function, which is based on PCA and multivariate curve resolution techniques. The visualization and data selection step involved manually selecting a wavenumber, which corresponds to a characteristic feature of PyC interlayer, and a *y*-coordinate to be used in the following steps. A wavenumber of 1500 cm^{-1} was used in this study; this wavenumber represents the shoulder of the carbon G-band. Spectral decomposition was performed on the acquired spectra using the open-source nonlinear

curve fitting program Fityk, with the peak characteristics optimized for the best fit using a combination of mixed Gaussian-Lorentzian profiles [62].

3. Results

3.1 Composite microstructure and characteristics of Raman spectra

Backscattered electron images for SiC/SiC composites are shown in Fig. 4. The scale of the images differs because SA3 and SCS have different fiber diameters. The diameters of the SA3 and SCS fibers are about 8 μm and 139 μm, respectively, and the thicknesses of the corresponding PyC interphase layers are about 0.3 μm and 0.9 μm. Free carbon phases, which were reported in literature [63], can be seen within the SA3 fibers. The SCS fibers contain a carbon core at the center but do not exhibit the fine particles seen in the SA3 fibers.

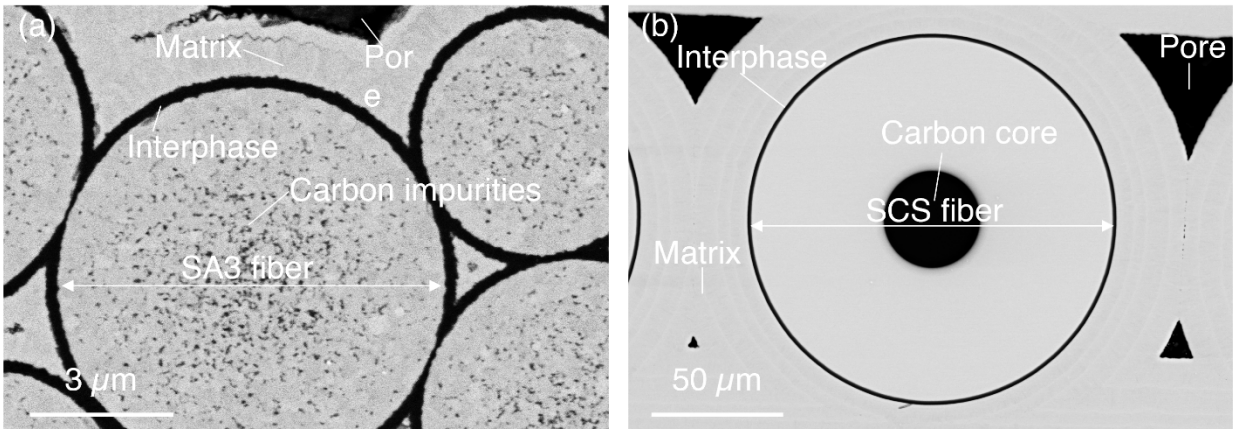

Fig. 4. Backscattered electron images for SiC/SiC composites with (a) Tyranno SA3 fiber, and (b) SCS-Ultra fiber.

Figures 5(a), (b), (c), and (d) show 3D displays of Raman spectra from the SA3/SiC and SCS/SiC composite materials as a function of the *x*-coordinate. The spectra corresponding to the positions indicated by red arrows in Figs. 5(c) and (d) are shown in Figs. 5(e) and (f), respectively. The optical phonon branches of 3C-SiC consist of two modes: LO mode located at 972 cm^{-1} and transverse optical (TO) mode located at 796 cm^{-1} [64,65]. Peaks corresponding to these modes can be seen in both the matrix and the fibers. In all cases, the TO peak exhibits an asymmetric shape, characterized either by a shoulder at 760–770 cm^{-1} or an adjacent peak at 785–790 cm^{-1}, which is attributed to overlap with disordered SiC peaks [22,64]. Additionally, a broad peak around 900 cm^{-1} reported as a disordered SiC peak [66] can be seen between the TO and LO peaks. These disordered SiC features can be associated with either randomly distributed simple polytype domains or SiC particles containing periodic or high-density stacking faults [63-65]. In the range of 400–600 cm^{-1}, peaks interpreted as Si–Si homonuclear bonds can be seen at nearly all locations [63]. Second-order SiC peaks are also observed at 1530 cm^{-1} and 1717 cm^{-1} [67,68]. These second-order SiC peaks partially overlap with carbon-related peaks in the 1200–1700 cm^{-1} range. The peaks observed in the 1200–1700 cm^{-1} range correspond to different carbon structures. The G-band, typically observed around 1580–1600 cm^{-1}, and the D-band, around 1350 cm^{-1}, are generally assigned to zone-center phonons of E_{2g} symmetry and K-point phonons of A_{1g} symmetry, respectively [69]. The G-band is associated with the bond-stretching motion of pairs of carbon sp^2 atoms, whereas the D-band is attributed to the breathing motion of sixfold aromatic rings. The G-band and D-band can both be seen at locations corresponding to the interphase, the SA3 fiber, and the matrix near the

interphase (i.e., $x \geq 1.4$ μm for the SA3/SiC and $-1.6 \leq x \leq 0.9$ μm for SCS/SiC). As shown in Fig.5(c) and (d), the SiC-related peaks reach a local minimum and the carbon-related peaks approach a local maximum at $x = 2.1$ μm for SA3/SiC and $x = -0.4$ μm for SCS/SiC. In the SCS/SiC composite, the absence of both SiC-TO and LO peaks, combined with the presence of carbon-related peaks, indicates that the Raman spectrum of PyC interphase was directly obtained. Notably, a consistent shoulder on the G-band at approximately 1500 cm^{-1} is seen at these interfacial positions.

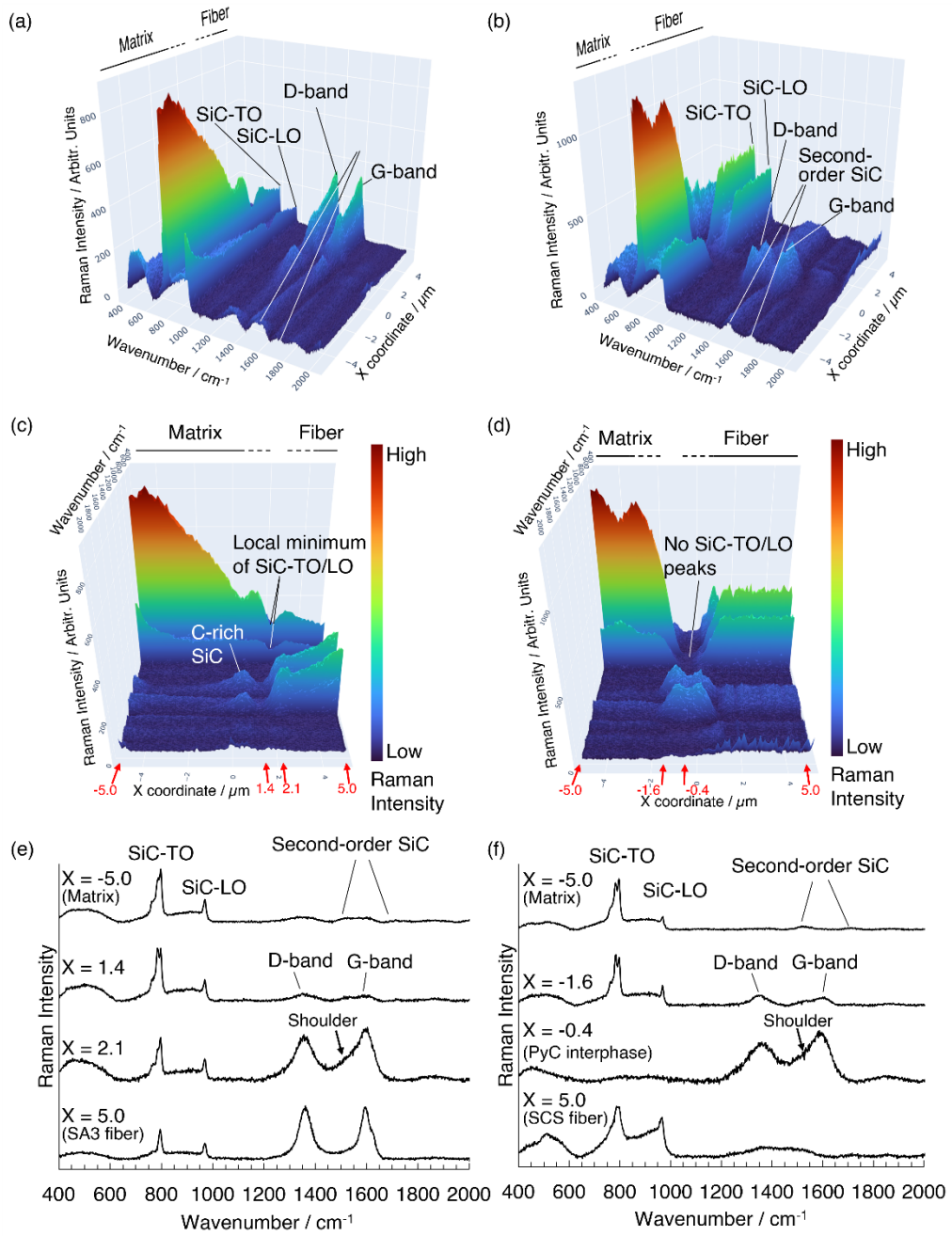

Fig. 5. Representative 3D display of spectral line analysis of Raman spectra along the *x*-axis for SiC/SiC composites with (a) Tyranno SA3 fiber and (b) SCS-Ultra fiber. Panels (c) and (d) show side views of (a) and (b), respectively. Representative Raman spectra for the composites with (e) Tyranno SA3 fiber and (f) SCS-Ultra fiber are displayed, with spectra normalized to the maximum intensity of the raw data. Red arrows indicate the positions of the representative spectra shown in (e) and (f).

3.2 Manual visualization of PyC interphase in Raman spectral images

To visualize the spatial regions exhibiting a shoulder on the G-band at approximately 1500 cm^{-1}, the Raman spectra were first normalized to the maximum intensity between 960 and 980 cm^{-1} (assigned to SiC-LO), followed by intensity mapping at 1500 cm^{-1}. Figure 6 shows both the normalized intensity map and the line profile along a representative *y*-coordinate. The region highlighted in the mapping displays a width of approximately 1 μm, which is slightly broader than the thickness of the PyC interphase observed in the optical microscope. Raman intensity profiles are consistent with the mapping views; line analyses shown in Fig. 6(a) and (b) reveal distinct intensity peaks within the approximately 1 μm wide interfacial region between the fiber and matrix.

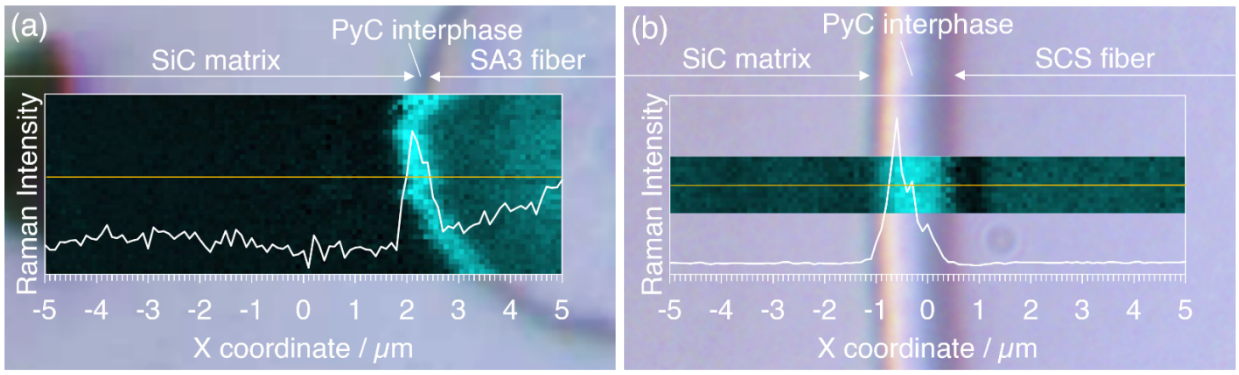

Fig. 6. Raman mapping images and line analysis results at wavenumber of 1500 cm^{-1} for SiC/SiC composites with (a) Tyranno SA3 fiber, and (b) SCS-Ultra fiber. Line analysis was performed along the horizontal orange line indicated in the overlaid mapping images.

3.3 Extraction of representative Raman spectrum of PyC phase

Figures 7(a) and (b) show the MAE as a function of the *x*-coordinate, illustrating the spatial relationships between the PyC interphase and surrounding phases as captured

by this spectral extraction method. These MAE profiles exhibit trends consistent with the line analysis results presented in Fig. 6. Raman spectra before and after extraction processing for SA3/SiC and SCS/SiC composites are shown in Figs. 7(c) and (d), respectively. The extracted PyC spectra display characteristic D-band (~1350 cm^{-1}) and G-band (~1600 cm^{-1}) features, with minimal influence from SiC related peaks between 700 and 1000 cm^{-1}. Notably, the PyC interphase spectra closely resemble those acquired at x = −0.4 μm in SCS/SiC composite, shown in Fig.5 (f), where the signal predominantly originates from the PyC interphase.

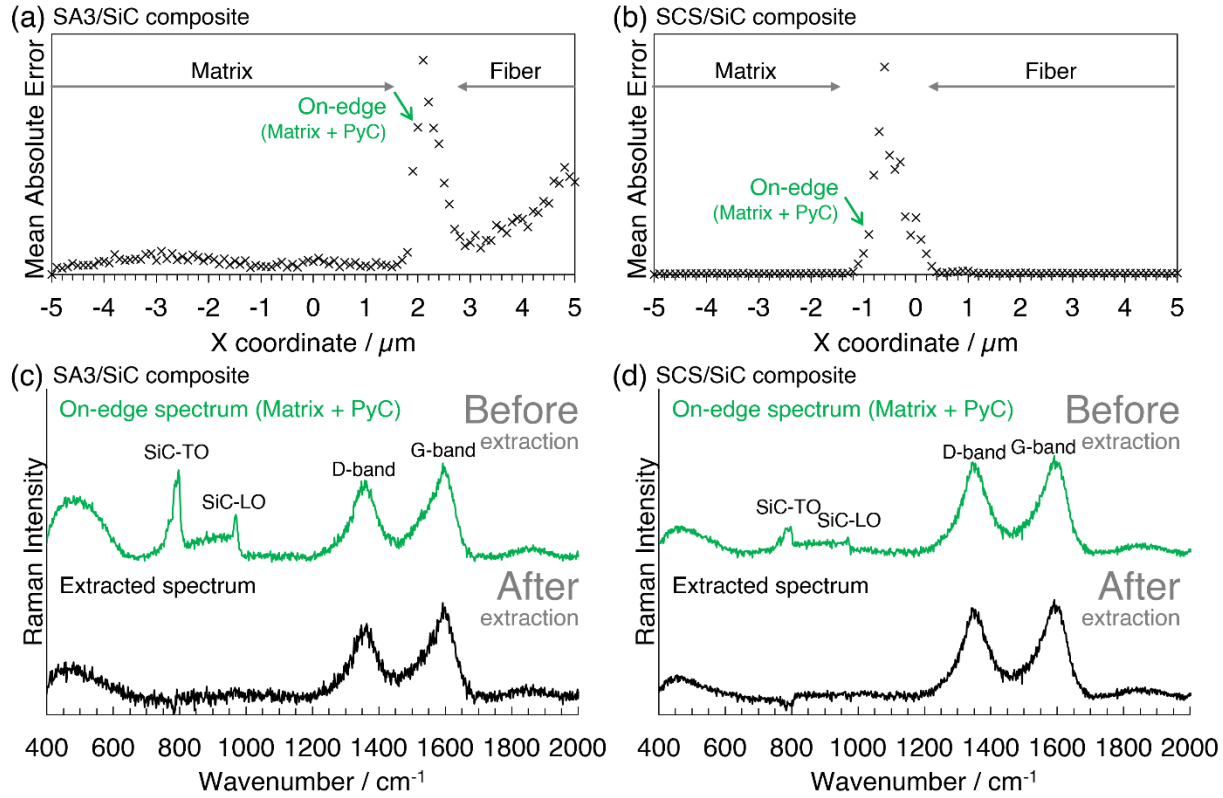

Fig. 7. MAE as a function of the x spatial coordinate for SiC/SiC composites with (a) Tyranno SA3 fiber and (b) SCS-Ultra fiber. Green arrows indicate the locations where spectral extractions (adjacent matrix spectrum subtracted) were performed. Raman spectrum before and after extraction for (c) SA3 composite, and (d) SCS composite. Spectra were normalized to their maximum intensity.

3.4 Conventional chemometrics of Raman spectral map data

The results from the extraction analysis in this study were compared to the chemometric analysis conducted using commercial software. Figures 8(a) and (b) show the spatial distributions of loadings obtained from χ-STaiN analysis on Raman spectral map for SA3/SiC and SCS/SiC composites, respectively. The χ-STaiN analysis identified three loadings for both composites. Loadings A, B, and C were interpreted based on spectral features corresponding to near matrix, interphase, and fibers, respectively. In the SCS/SiC composite, loading B exhibits a strong correlation to the intensity mapping at 1500 cm^{-1} shown in Fig. 6(b). For the SA3 composite, loading B covers a broader region than that highlighted in the corresponding mapping in Fig. 6(a), spanning about 3 μm. This is consistent with the width of the carbon-rich matrix and interphase shown in Fig. 5(c). The spectral characteristics of the χ-STaiN loadings for SA3/SiC and SCS/SiC composites are shown in Figs. 8(c) and (d), overlaid with representative spectra from corresponding coordinates. For the SCS/SiC composite, loading B closely matches the constituent spectrum extracted for the PyC interphase. In the SA3/SiC composite, the χ-STaiN-calculated loading retains peaks associated with the SiC, which is not contained in PyC. Loading A and C match all significant peaks with the corresponding spectra of matrix and fiber, including SiC-TO, LO, D-band, and G-band.

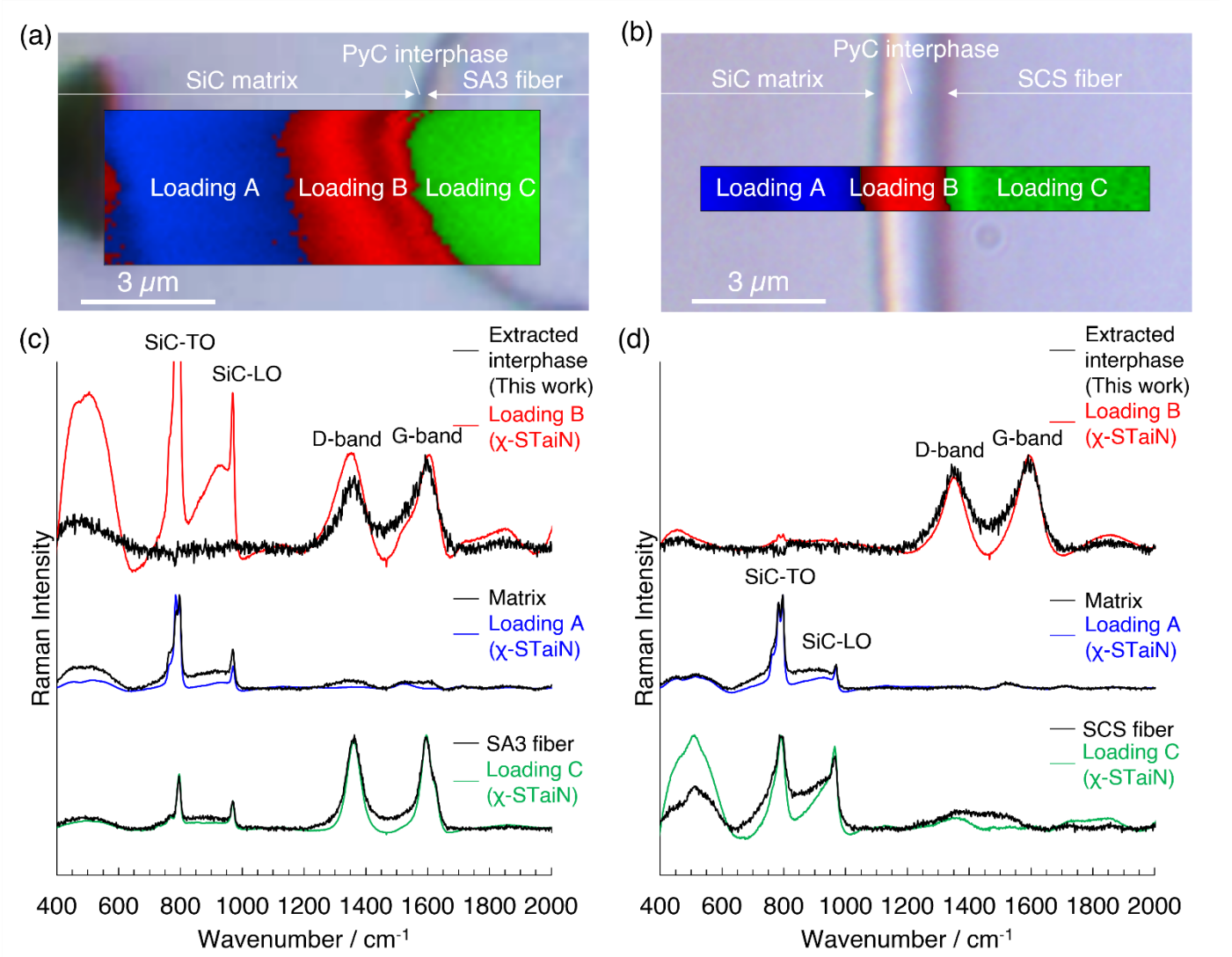

Fig. 8. χ-STaiN loading maps of SiC/SiC composites with (a) Tyranno SA3 fiber and (b) SCS-Ultra fiber. Raman spectra showing the extracted PyC interphase, matrix, fiber, and χ-STaiN loadings corresponding to each phase of SiC/SiC composites with (c) Tyranno SA3 fiber and (d) SCS-Ultra fiber.

4. Discussion

This method to extract the Raman spectrum of sub-micrometer thick PyC interphases from the mixed spectrum takes advantage of the small step size in the mapped data and the relatively strong PyC signals compared to the second-order SiC peaks, based

on the procedure shown in Fig. 3. Notably, the conventional chemometrics procedures available in the commercial software package could not extract the PyC spectrum and instead showed a mixed spectrum as a principal component because of the lack of consideration for the spatial resolution of the measurements (Fig. 8). The following subsection discusses the validation and general applicability of the spectrum extraction method to other material systems.

4.1 Validation of the Raman analysis approach

This study used the SCS/SiC composite specimen for data validation. The Raman spectrum of the PyC interphase could be directly measured via point analysis because the interphase thickness is greater than the theoretical laser spot size (Fig. 5(f), x = −0.4 μm). Figure 9(a) shows the Raman spectrum originating from PyC interphase and the extracted PyC interphase spectrum measured from SCS/SiC composites. The extracted spectrum retains the main spectral features of PyC interphase, yielding a cosine similarity of 0.984 (where 1 indicates a perfect match). Differential intensity plots reveal mismatch peaks at D-band and approximately 1500 cm^{-1}, with intensities of approximately −15% and 15%. These discrepancies arise from multiple factors, including signal intensity fluctuations of about ±10% and distortions in the broad-band region caused by background subtraction. A polynomial-fitted baseline was subtracted from the raw spectra, which can distort the edges of broad bands – a distortion evident in increased differential intensity at off-peak regions. Despite these effects, the differential intensity variation of ±15% is relatively minor, indicating that the effective spectral deviation remains small.

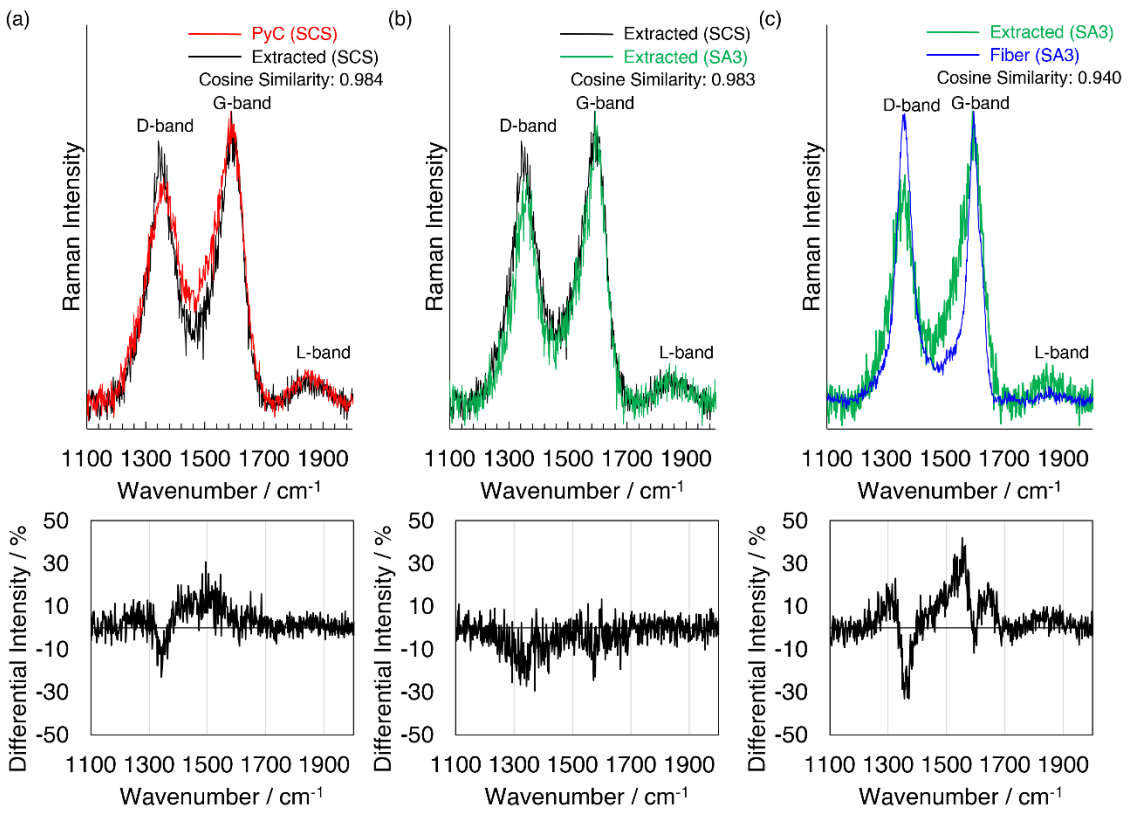

Fig. 9. Spectral comparisons of Raman data: (a) between the PyC interphase (x = −0.4 μm) and the extracted spectrum from the SCS/SiC composite, (b) between the extracted spectra from the SCS/SiC and SA3/SiC composites, and (c) between the SA3 fiber and the extracted spectrum from the SA3/SiC composite. All Raman spectra are normalized to the maximum intensity of G-band (within the 1590–1610 cm^{-1} range). Differential intensities, expressed as percentages relative to the maximum G-band intensity, are shown below each respective comparison.

Indirect validations of the extraction method of the PyC spectrum from the SA3/SiC composite specimen were performed. One approach involved comparing the extracted PyC spectra from the SCS/SiC and SA3/SiC composite specimens. Similar Raman features were expected between the two because they were deposited by the same company in the same batch. The extracted spectra of PyC interphase of SA3/SiC and SCS/SiC composites are summarized in Fig. 9(b). The spectra were normalized to the maximum intensity of the raw spectra in the range of 1580–1600 cm^{-1} (G-band).

Extracted interphase spectra from SCS/SiC and SA3/SiC both show the D-, G-, and L-band overlapping at approximately 1350, 1600, and 1850 cm^{-1}, respectively, yielding a cosine similarity of 0.983. Differential intensity indicates a peak at the D-band with an intensity of about 20%, whereas no peaks or peaks indistinguishable from noise are observed at the other wavenumbers. Given the close match of the extracted spectra of SA3/SiC and SCS/SiC composites, the extracted spectrum from SA3/SiC likely preserves the characteristics of PyC interphase.

The PyC spectrum extracted from the SA3/SiC composite was compared with the carbon-related spectrum obtained from the interior of an SA3 fiber. The PyC phase is expected to exhibit unique Raman features not present in the SCS and SA3 fibers, as indicated by the Raman intensity map shown in Fig. 6. Figure 9(c) presents both the extracted PyC spectrum and the spectrum from the SA3 fiber interior (measured at x = 5.0 μm in Fig. 5(e)). The extracted PyC spectrum exhibits reduced D-band intensity, increased G-band dispersion, and the presence of the L-band, features not prominent in the fiber spectrum. The intensity of the broader G-band also increases near 1500 cm^{-1}, assisting in interphase localization. These spectral differences can be seen in the differential intensity curve, which displays peaks between 1200 and 1700 cm^{-1}, with a maximum absolute intensity of 42%. The cosine similarity is 0.940, lower than the values observed in Figs. 9(a) and (b). These spectral differences indicate that the extracted PyC spectrum is distinct from that of the SA3 fiber interior. Together, these results support the validity of the extraction method for identifying the PyC interphase in the SA3/SiC composite.

4.2 Interpretation of the extracted Raman spectra

As shown in Fig. 9(a), the extracted spectrum exhibits a slightly higher D-band intensity and slightly reduced D- and G-band dispersions compared to the directly measured PyC, suggesting a marginally higher degree of order in the carbon structure. This result may be explained by slight variations in the reference matrix and PyC spectrum at different locations. For example, localized graphitization at the edge of the PyC may have occurred during the CVI process of SiC matrix, consistent with observations by López-Honorato et al. [70]

Peak fitting showed that all spectra from interphases and fibers had one major peak between 1351 and 1372 cm^{-1} corresponding to the D-band [71], as shown in Fig.10. SA3 fiber, SA3/SiC interphase, and SCS/SiC interphase all exhibit another major peak around 1600 cm^{-1} associated with the G-band [71]. SCS fiber exhibits a second major peak at 1501 cm^{-1}, also associated with the G-band [69]. The spectrum of SCS fiber is characterized by broad peaks and a red-shifted G-band; these features can be interpreted as characteristics of amorphous carbon [30] or hydrogenated amorphous carbon [31]. A peak at 1723 cm^{-1} can be interpreted as benzene-related stretching [72]. The features found in SCS are consistent with those observed near the core of the same fiber [8].

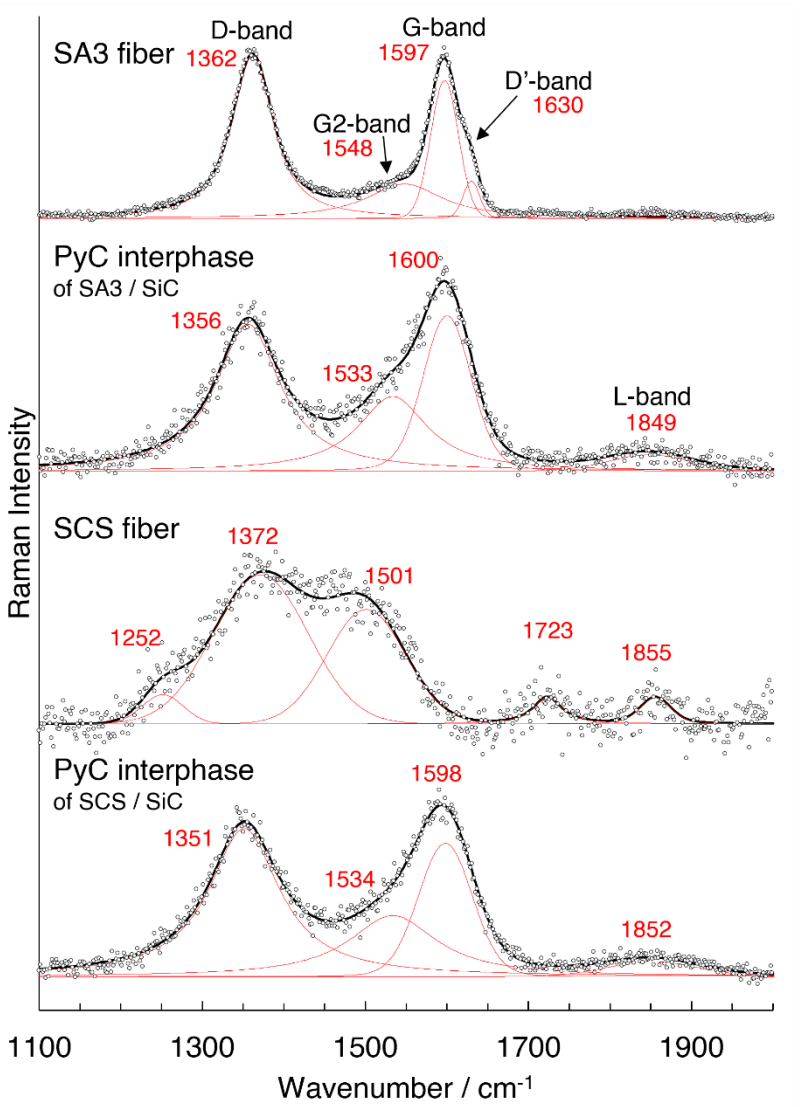

Fig. 10. Raman spectra for the extracted interphases and fibers. The spectra are normalized to the maximum intensity of the raw spectra of the D-band (within the range of 1345–1375 cm^{-1}). Plots, black lines, and red lines represent raw spectra, calculated model curves, and the individual components of the models, respectively. Peak centers are indicated beside each component.

A comparative analysis of the Raman spectra of SA3 fiber and its adjacent PyC interphase revealed spectral similarity. Specifically, both spectra contained a D-band, G-band, and G2-band at approximately 1530 cm^{-1}, forming a shoulder on the G-band. The intensity ratio between D- and G-band was approximately 1.2 for the SA3 fiber and

0.9 for the PyC interphase. The G2-bands were observed at around 1548 cm^{-1} in the SA3 fiber and 1533 cm^{-1} in the interphase; these bands are attributed to sp^2 carbon clusters resembling those found in amorphous carbon film [73].

The peak fitting revealed distinct structural differences between SA3 and PyC, including an overlapping peak at 1630 cm^{-1}, an additional peak at 1850 cm^{-1}, variations in G-band width, and a shift in D-band peak position. The SA3 fiber spectrum exhibited an additional peak, overlapping the G-band and centered at 1630 cm^{-1}, called the D′-band. The D′-band is associated with the folding of the graphite dispersion branch at the Γ point and indicates turbostratic disorder along the *c*-axis based on the literature [74]. This D′-band is consistent with previously reported Raman spectra of SA3 fibers [63]. The extracted PyC interphases did not show a shoulder due to the D′-band, but did exhibit D- and G-bands with features consistent with PyC [12,70]. Although both SA3 and PyC showed peaks corresponding to the D-band, the peak center for PyC interphase was red-shifted by 6 cm^{-1}. This shift suggests a reduction in the number of ordered aromatic rings and a softening of the vibrational density of states within the interphase carbon [69]. Furthermore, the peak corresponding to the G-band for PyC was broader than that for SA3, indicating an increased degree of disorder [69]. The full width at half maximum of the G-bands were 58 cm^{-1} for PyC interphase and 39 cm^{-1} for SA3 fiber. Consequently, the G-band for PyC almost completely overlapped the peak at 1533 cm^{-1}, forming a characteristic shoulder in the Raman spectral profile of PyC interphase. Additionally, PyC interphases from SA3/SiC and SCS/SiC composites

indicated peaks at 1849 cm^{-1} and 1852 cm^{-1}, respectively, which are interpreted as so-called L-band corresponding to 1D chains of carbon atoms [75,76].

Taken together, the carbon-related Raman features of the PyC interphase were distinguishable from those of the adjacent SA3 fiber based on key characteristics such as the presence of peaks and the profile of D- and G-bands. The carbon in the SA3 fiber indicated the presence of turbostratic carbon corresponding to the peak at 1630 cm^{-1}, and that in the PyC interphase had more disordered microstructures represented by the red-shifted D-band and broader G-band. Carbon in PyC can be identified as non-graphitizing carbon with a higher degree of disorder than that in SA3 [12,77]. SA3 fiber contains turbostratic carbon at the triple points of SiC crystals [32,54]. PyC interphase is deposited by CVD using methane, polypropylene, or propane as the carbon source [78-80] and is deposited on a cylinder, so misalignment of the crystallites is plausible [70].

4.3 Application of the analysis method for other material systems

The spectral extraction method presented in this study offers several practical advantages over other approaches for enhancing spatial resolution in Raman spectroscopy. It is compatible with conventional Raman spectrometers, applicable to existing mapping datasets, computationally efficient, and can be integrated with other analytical tools such as image recognition algorithms and chemometric techniques. Because the method operates on hyperspectral Raman data after measurement, no

hardware modifications are necessary, and previously acquired data can be reanalyzed, assuming adequate spatial resolution.

The spectrum extraction method used in this study relies on the availability of a reference Raman spectrum of the surrounding matrix, which enables the extraction of Raman features of thin interphases embedded in mixed spectra. Additionally, the pixel spacing of Raman spectral maps must be finer than the thickness of the interphase. For instance, in this study, the nominal step size of 0.1 μm was used to analyze an approximately 0.3 μm thick interphase. A minimum of three data points across the interphase thickness was required to obtain sufficient intensity of PyC in the mixed spectrum. If these conditions are met, then the extraction methodology is expected to work for other material systems with thin interphases. A primary challenge arises when the interphase is a gradient material with a heterogeneous microstructure and the Raman profile of the matrix varies spatially. This situation causes the absence of a consistent reference peak for the extraction process.

An additional consideration is that the effective sampling depth in Raman mapping can vary spatially due to differences in the optical properties of the constituent phases and the relative intensities of their Raman signals. Phases with strong Raman activity, such as carbon, may dominate the measured spectrum and suppress contributions from adjacent or underlying phases[81,82]. If the micro-region of interest consists of such a strongly Raman-active phase, as in this case, this effect can facilitate the extraction. However, if the strongly scattering phase is part of the matrix rather than the micro-

region, the Raman contribution from the micro-region may become comparatively weak, making extraction more difficult. This highlights the importance of ensuring sufficient Raman signal intensity from the micro-region of interest.

Beyond thin layers, this method can also be extended to materials with dispersed fine particles based on the same principles. Moreover, this approach could be extended to material systems beyond SiC/SiC composites with a PyC interphase, particularly for cases in which spectral overlap between constituent materials is minimal or absent. For instance, spectral separation may be achievable in SiC/SiC composites employing boron nitride as the interphase. Boron nitride exhibits an E_{2g} mode peak at approximately 1365 cm^{-1} under 532 nm excitation light [83]; this peak overlaps with the D-band from carbon impurity in SA3 fiber. By carefully selecting the on-edge point on the matrix side, the interphase spectrum may be extracted using a similar methodology to that presented in this study.

Improving the spatial resolution of Raman spectral analysis is a topical area. For example, Raman spectroscopy integrated with SEM [84,85] can be used to analyze fine microstructural features at the scale of SEM imaging. The higher resolution SEM imaging compared with the Raman hyperspectral data facilitates interpretation of the chemical and structural information of Raman spectra and their correlation with morphology. A key direction for future improvement of Raman spectral map analysis is

the chemometrics-based analysis informed by both the spatial resolution of the Raman mapping and contrasts in specimen surface images. Combining this spectral extraction method with Raman spectral imaging techniques, including PCA and multivariate curve resolution, promises to improve spectral separation, especially by avoiding reduction in the signal-to-noise ratio [86], and allows for identification of materials currently indistinguishable due to noise. Consequently, the potential of the method would be enhanced for analyzing micro-regions observed with high-resolution imaging techniques, including SEM.

5. Conclusions

This study addressed the challenges in extracting the Raman spectrum of thin carbon interphase from the mixed spectrum of SiC and carbon phases. By leveraging the small 0.1 μm step size for the Raman mapping, the characteristic Raman spectrum of approximately 0.3 μm thick PyC interphase was extracted using the data obtained with a theoretical spot size of about 0.7 μm. Importantly, conventional chemometrics procedures could not extract the spectrum of the interphase and instead presented a mixed spectrum as a principal component. Different SiC composite specimen with approximately 0.9 μm thick PyC interphase was used to develop the analysis framework. The analysis revealed that carbon-related peaks of the extracted PyC spectra were distinct from those of free carbon phases in the SiC fibers due to the different manufacturing routes. Overall, the key to improving interpretation of the Raman spectral map data with mixed phases was to conduct Raman analysis informed by hyperspectral data with fine pixel spacing and contrast of the optical microscope

images. This study also identified the requirements to apply the extraction methodology such as ratio of the interphase thickness to the laser spot size and homogeneity of the matrix spectrum at different locations. If those requirements are met, then this method has potential to be applied to other composite material systems.

Acknowledgments

This work was supported by the US Department of Energy Office of Nuclear Energy, Advanced Fuels Campaign and Office of Fusion Energy Sciences, Fusion Materials Program and Early Career Research Program under Contract No. DE-AC05-00OR22725 with UT-Battelle, LLC. The authors wish to thank Chad Parish, Jose' Arregui Mena, and Erica Heinrich at ORNL for reviewing and editing this manuscript.

References

1. Naslain RR, *Composites, Part A* **1998**; *29* 1145-1155.
2. Snead LL, Nozawa T, Katoh Y, Byun T-S, Kondo S, Petti DA, *J. Nucl. Mater.* **2007**; *371* 329-377.
3. Kaya H, *Compos. Sci. Technol.* **1999**; *59* 861-872.
4. Murthy PLN, Nemeth NN, Brewer DN, Mital S, *Composites, Part B* **2008**; *39* 694-703.
5. Wang X, Gao X, Zhang Z, Cheng L, Ma H, Yang W, *J. Eur. Ceram. Soc.* **2021**; *41* 4671-4688.
6. Katoh Y, Snead LL, *J. Nucl. Mater.* **2019**; *526*.
7. Nozawa T, Hinoki T, Hasegawa A, Kohyama A, Katoh Y, Snead LL, Henager CH, Hegeman JBJ, *J. Nucl. Mater.* **2009**; *386-388* 622-627.
8. Koyanagi T, Katoh Y, *J. Nucl. Mater.* **2017**; *494* 46-54.
9. Yang W, Araki H, Noda T, Park JY, Katoh Y, Hinoki T, Yu J, Kohyama A, *Mater. Trans., JIM* **2002**; *43* 2568-2573.
10. Yang W, Araki H, Noda T, Hu Q, Suzuki H, Katoh Y, Kohyama A, in *Advanced SiC/SiC Ceramic Composites: Developments and Applications in Energy Systems* **2002**, pp. 273-280.

11. Li Z, Li X, Zhang B, Zhou X, Liu C, Jiang Y, Zhen C, Zheng C, Zhang L, Cheng L, *Ceram. Int.* **2020**; *46* 18071-18078.
12. Stein IY, Constable AJ, Morales-Medina N, Sackier CV, Devoe ME, Vincent HM, Wardle BL, *Carbon* **2017**; *117* 411-420.
13. Katoh Y, Nozawa T, Snead LL, *J. Am. Ceram. Soc.* **2005**; *88* 3088-3095.
14. Nozawa T, Koyanagi T, Katoh Y, Tanigawa H, *J. Eur. Ceram. Soc.* **2019**; *39* 2634-2647.
15. Karakoc O, Koyanagi T, Nozawa T, Katoh Y, *Composites, Part B* **2021**; *224*.
16. Yan JY, Chen CW, Fang PC, Yin KM, Chen FR, Katoh Y, Kohyama A, Kai JJ, *J. Nucl. Mater.* **2004**; *329-333* 513-517.
17. Agarwal S, Duscher G, Zhao Y, Crespillo ML, Katoh Y, Weber WJ, *Acta Mater.* **2018**; *161* 207-220.
18. Yan Z, Feng Q, Zheng J, Guo X, Zhang X, Zhang S, Mi X, Xue J, Yan Y, Ge H, Wang G, Zhu Z, Zhou W, *Ceram. Int.* **2025**; *51* 12082-12094.
19. Gu G, Schnatterly SE, *Phys. Rev. B:Condens. Matter Mater. Phys.* **1995**; *52* 5298-5301.
20. Nueangnoraj K, Nishihara H, Imai K, Itoi H, Ishii T, Kiguchi M, Sato Y, Terauchi M, Kyotani T, *Carbon* **2013**; *62* 455-464.
21. Marcus B, Fayette L, Mermoux M, Abello L, Lucazeau G, *J. Appl. Phys.* **1994**; *76* 3463-3470.
22. Nakashima Si, Higashihira M, Maeda K, Tanaka H, *J. Am. Ceram. Soc.* **2003**; *86* 823-829.
23. Tuinstra F, Koenig JL, *J. Chem. Phys.* **1970**; *53* 1126-1130.
24. Sasaki Y, Nishina Y, Sato M, Okamura K, *Phys. Rev. B:Condens. Matter Mater. Phys.* **1989**; *40* 1762-1772.
25. Krishna R, Jones AN, Edge R, Marsden BJ, *Radiat. Phys. Chem.* **2015**; *111* 14-23.
26. Olego D, Cardona M, Vogl P, *Phys. Rev. B* **1982**; *25* 3878-3888.
27. Gouadec G, Colomban P, Bansal NP, *J. Am. Ceram. Soc.* **2001**; *84* 1136-1142.
28. Gouadec G, Karlin S, Wu J, Parlier M, Colomban P, *Compos. Sci. Technol.* **2001**; *61* 383-388.
29. Gouadec G, Colomban P, *J. Eur. Ceram. Soc.* **2001**; *21* 1249-1259.
30. Schwan J, Ulrich S, Batori V, Ehrhardt H, Silva SRP, *J. Appl. Phys.* **1996**; *80* 440-447.
31. Tamor MA, Vassell WC, *J. Appl. Phys.* **1994**; *76* 3823-3830.
32. Havel M, Colomban P, *J. Raman Spectrosc.* **2003**; *34* 786-794.
33. Havel M, Baron D, Colomban P, *J. Mater. Sci.* **2004**; *39* 6183-6190.
34. Abbe E, *J. R. Microsc. Soc.* **1883**; *3* 790-812.
35. Maznev AA, Wright OB, *Wave Motion* **2017**; *68* 182-189.
36. Anderson MS, *Appl. Phys. Lett.* **2000**; *76* 3130-3132.
37. Stöckle RM, Suh YD, Deckert V, Zenobi R, *Chem. Phys. Lett.* **2000**; *318* 131-136.
38. Makki AA, Bonnier F, Respaud R, Chtara F, Tfayli A, Tauber C, Bertrand D, Byrne HJ, Mohammed E, Chourpa I, *Spectrochim Acta A Mol Biomol Spectrosc* **2019**; *218* 97-108.

39. Peng W, Beggio G, Pivato A, Zhang H, Lü F, He P, *Renewable and Sustainable Energy Reviews* **2022**; *165*.
40. Chavent M, Guégan H, Kuentz V, Patouille B, Saracco J, *Environmetrics* **2008**; *20* 928-942.
41. Caggiani MC, Colomban P, *J. Raman Spectrosc.* **2023**; *55* 116-124.
42. Coccato A, Caggiani MC, *J. Raman Spectrosc.* **2023**; *55* 125-147.
43. Campos JLE, Miranda H, Rabelo C, Sandoz-Rosado E, Pandey S, Riikonen J, Cano-Marquez AG, Jorio A, *J. Raman Spectrosc.* **2017**; *49* 54-65.
44. Ilie AG, Scarisoareanu M, Morjan I, Dutu E, Badiceanu M, Mihailescu I, *Appl. Surf. Sci.* **2017**; *417* 93-103.
45. Maslova OA, Guimbretière G, Ammar MR, Desgranges L, Jégou C, Canizarès A, Simon P, *Mater. Charact.* **2017**; *129* 260-269.
46. Abdi H, Williams LJ, *WIREs Comput. Stat.* **2010**; *2* 433-459.
47. Shinzawa H, Awa K, Kanematsu W, Ozaki Y, *J. Raman Spectrosc.* **2009**; *40* 1720-1725.
48. Eckart C, Young G, *Psychometrika* **1936**; *1* 211-218.
49. Parastar H, Jalali-Heravi M, Tauler R, *TrAC, Trends Anal. Chem.* **2012**; *31* 134-143.
50. Zhang L, Henson MJ, Sekulic SS, *Anal. Chim. Acta* **2005**; *545* 262-278.
51. Vajna B, Patyi G, Nagy Z, Bódis A, Farkas A, Marosi G, *J. Raman Spectrosc.* **2011**; *42* 1977-1986.
52. Kunc J, Hu Y, Palmer J, Berger C, de Heer WA, *Appl. Phys. Lett.* **2013**; *103*.
53. de Juan A, Jaumot J, Tauler R, *Anal. Methods* **2014**; *6* 4964-4976.
54. Sauder C, Lamon J, *J. Am. Ceram. Soc.* **2007**; *90* 1146-1156.
55. Braun J, Fellah C, Labrugère C, Vaudescal M, Sauder C, *Int. J. Appl. Ceram. Technol.* **2024**; *22*.
56. Yugami H, Nakashima S, Mitsuishi A, Uemoto A, Shigeta M, Furukawa K, Suzuki A, Nakajima S, *J. Appl. Phys.* **1987**; *61* 354-358.
57. Chollon G, Naslain R, Prentice C, Shatwell R, May P, *J. Eur. Ceram. Soc.* **2005**; *25* 1929-1942.
58. Vandenabeele P *Practical Raman Spectroscopy – An Introduction*; John Wiley & Sons, Ltd: Hoboken, 2013.
59. Young RJ, Broadbridge AB, So C, *J. Microsc.* **1999**; *196* 257-265.
60. Willmott CJ, Matsuura K, *Chlim. Res.* **2005**; *30* 79-82.
61. Jimba Y, Lamm B, Koyanagi T, "Interphase Extractor at GitHub" https://github.com/jimba-y/InterphaseExtractor (Accessed: 30 June 2025)
62. Wojdyr M, *J. Appl. Crystallogr.* **2010**; *43* 1126-1128.
63. Huguet-Garcia J, Jankowiak A, Miro S, Gosset D, Serruys Y, Costantini JM, Vance L, *J. Am. Ceram. Soc.* **2014**; *98* 675-682.
64. Nakashima S, Harima H, *Phys. Status Solidi A* **1997**; *162* 39-64.
65. Rohmfeld S, Hundhausen M, Ley L, *Phys. Status Solidi B* **1999**; *215* 115-119.
66. Sreelakshmi N, Amirthapandian S, Umapathy GR, David C, Srivastava SK, Ojha S, Panigrahi BK, *Mater. Sci. Eng. B* **2021**; *273*.
67. Sorieul S, Costantini JM, Gosmain L, Thomé L, Grob JJ, *J. Phys.:Condens. Matter* **2006**; *18* 5235-5251.

68. Miro S, Costantini JM, Sorieul S, Gosmain L, Thomé L, *Philos. Mag. Lett.* **2012**; *92* 633-639.
69. Ferrari AC, Robertson J, *Phys. Rev. B* **2000**; *61* 14095.
70. López-Honorato E, Meadows PJ, Shatwell RA, Xiao P, *Carbon* **2010**; *48* 881-890.
71. Havel M, Colomban P, *Composites, Part B* **2004**; *35* 139-147.
72. Chen ZY, Zhao JP, Yano T, Ooie T, Yoneda M, Sakakibara J, *J. Appl. Phys.* **2000**; *88* 2305-2308.
73. Shimodaira N, Masui A, *J. Appl. Phys.* **2002**; *92* 902-909.
74. Colomban P, Gouadec G, Mazerolles L, *Mater. Corros.* **2002**; *53* 306-315.
75. Ando Y, Zhao X, Kataura H, Achiba Y, Kaneto K, Uemura S, Iijima S, *Trans. Mater. Res. Soc. Jpn.* **2000**; *25* 817-820.
76. Zhao X, Ando Y, Liu Y, Jinno M, Suzuki T, *Phys. Rev. Lett.* **2003**; *90* 187401.
77. Franklin RE, *Proc. R. Soc. A* **1951**; *209* 196-218.
78. Rawlins MH, Nolan TA, Stinton DP, Lowden RA, *Mater. Res. Soc. Symp. Proc.* **1987**; *78* 223-230.
79. Fischbach DB, Lemoine PM, *Compos. Sci. Technol.* **1990**; *37* 55-61.
80. Liaw PK, *JOM* **1995**; *47* 38-44.
81. Caggiani MC, Colomban P, *Phys. Sci. Rev.* **2018**; *3* 20180007.
82. Gouadec G, Bellot-Gurlet L, Baron D, Colomban P, in *Raman Imaging*; (Ed Zoubir A); Springer, Berlin, Heidelberg: **2012**, pp. 85-118.
83. Chen X, Cheng G, Yang J, Hu J, Liao C, Zhang X, Dong S, *J. Adv. Ceram.* **2021**; *11* 94-104.
84. Liu F, Zou X, Yue N, Zhang W, Zheng W, *Cell Rep. Phys. Sci.* **2023**; *4*.
85. Schmidt R, Nachtnebel M, Dienstleder M, Mertschnigg S, Schroettner H, Zankel A, Poteser M, Hutter HP, Eppel W, Fitzek H, *Micron* **2021**; *144* 103034.
86. Peris-Díaz MD, Krężel A, *TrAC, Trends Anal. Chem.* **2021**; *135*.